Journal of Materials Chemistry A

Operando Structural and Chemical Evolutions of TiS2 in Na-ion Batteries

Journal:	*Journal of Materials Chemistry A*
Manuscript ID	TA-ART-01-2020-000226.R1
Article Type:	Paper
Date Submitted by the Author:	31-Mar-2020

Complete List of Authors:	Lin, Cheng-Hung; Stony Brook University, Materials Science and Chemical Engineering Topsakal, Mehmet; Brookhaven National Laboratory, Nuclear Science and Technology Sun, Ke; Stony Brook University, Materials Science and Chemical Engineering; Brookhaven National Laboratory, Sustainable Energy Technologies Bai, Jianming; Brookhaven National Laboratory, National Synchrotron Light Source II Zhao, Chonghang; Stony Brook University, Dooryhee, Eric; Brookhaven National Laboratory, National Synchrotron Light Source II Northrup, Paul; Stony Brook University, Department of Geosciences Gan, Hong; Brookhaven National Laboratory, Sustainable Energy Technologies Lu, Deyu; Brookhaven National Laboratory, Center for Functional Nanomaterials Stavitski, Eli; Brookhaven National Laboratory, National Synchrotron Light Source II Chen-Wiegart, Yu-chen Karen; Stony Brook University, Materials Science and Chemical Engineering; Brookhaven National Laboratory,

Operando Structural and Chemical Evolutions of TiS_2 in Na-ion Batteries

Cheng-Hung Lin[1], Mehmet Topsakal[2], Ke Sun[1, 3], Jianming Bai[4], Chonghang Zhao[1], Eric Dooryhee[4], Paul Northrup[5], Hong Gan[3], Deyu Lu[6], Eli Stavitski[4], Yu-chen Karen Chen-Wiegart[1, 4]

1. Department of Materials Science and Chemical Engineering, Stony Brook University, Stony Brook, NY 11794
2. Nuclear Science and Technology Department, Brookhaven National Laboratory, Upton, NY 11973
3. Sustainable Energy Technologies Department, Brookhaven National Laboratory, Upton, NY 11973
4. National Synchrotron Light Source II, Brookhaven National Laboratory, Upton, NY 11973
5. Department of Geosciences, Stony Brook University, Stony Brook, NY, 11794
6. Center for Functional Nanomaterials, Brookhaven National Laboratory, Upton, NY 11973

Abstract:

Titanium disulfide (TiS_2) with high electric conductivity, fast rate capability, and good cycling performance is a promising candidate of electrode material for sodium (Na)-ion batteries. Despite the well-studied electrochemical behaviors of TiS_2 in Li-ion batteries, the detailed reaction mechanism of TiS_2 in Na-ion batteries is not yet fully understood due to a more complex multi-phase conversion process. In this work, battery reactions of TiS_2 in Na-ion are investigated via a multi-modal synchrotron approach: *operando* X-ray Absorption Spectroscopy (XAS) – including X-ray Absorption Near Edge Structure (XANES) and Extended X-ray Absorption Fine Structure (EXAFS) - and *ex situ* X-ray Powder Diffraction (XPD), coupled with computational modeling. *Operando* XANES spectra indicate the redox reactions occur in both Ti and S during the electrochemically driven phase transformation. Multivariate Curve Resolution - Alternating Least Squares (MCR-ALS) analysis of XAS suggests different numbers of components are involved in lithiation and sodiation of TiS_2, with the sodiation includes at least one intermediate phase in addition to the starting material and final sodiation product. *Ex situ* XPD and Rietveld refinement further determined and quantified the unknown phases – showing that three phases, TiS_2, $Na_{0.55}TiS_2$, and $NaTiS_2$, participate in sodiation of TiS_2. *Operando* EXAFS results show the changes of Ti-Ti coordination number and interatomic distance. This explains the Coulombic efficiency decay due to the incomplete recovery of coordination number of Ti after cycling. Overall, this work reveals the reaction mechanism occurring in Na-TiS_2 batteries with greater quantitative understanding on the structural evolution. By combining multi-modal synchrotron approach and computational work, this study provides a framework for studying a broader range of electrochemically driven phase-transformation systems towards advanced energy storage and conversion applications.

1. Introduction

Larger scale of energy storage, such as electric vehicle (EV) and intermittent sustainable energy for electrical grid, attracts an accumulating research interest and booming investment in recent years. A large research gap remains for current lithium ion batteries (LIBs) to satisfy the demands of large-scale storage. The battery technology continues advancing to increase energy density, stability and safety at reduced cost. Today, cobalt/nickel-based metal oxides, such as $LiCoO_2$, $LiNi_xCo_yMn_zO_2$, and $LiNi_{0.53}Co_{0.3}Al_{0.17}O_2$, dominate the cathode materials in commercial lithium coin cell.[1] However, to reduce the cost and achieve a better performance,[2] researchers continue searching potential alternative electrodes.

Layered transition metal dichalcogenides (MX_2; M=transition metal, X=S, Se, Te) provide another promising direction for intercalation of host species in cathodes. Titanium disulfide (TiS_2) has been studied extensively since its kinetically favorable insertion reaction in alkali metals was reported by Whittingham in 1976.[3] Because of its good electric conductivity,[4] higher energy density than $LiCoO_2$, and rapid cycling rate,[4] TiS_2 is now considered as a strong contender in LIB as well as beyond Li-ion, such as Na, K, and Mg for the application of high power systems.[5-7] Moreover, TiS_2 provides a possibility to be incorporated with metal lithium anode for an all-solid-state cell and acts as an absorber of Li-polysulfides in lithium-sulfur battery to enhance cell performance.[8]

Therefore, upon considering the abundance of transition metals and alkali metals (titanium ~0.1% and sodium ~ 2%), TiS_2-based systems in Na battery show a high potential for the next generation energy storage.[9-11] Despite the benefits of Na-TiS_2 system, using TiS_2 as an intercalation host for cathode still faces challenges. In particular, the lack of knowledge of TiS2 structural and chemical evolution in the Na battery hinders the development of this new-type energy storage system.[6, 12-15] Intercalation of Li into TiS_2 layers occurs without changes in the crystalline structure. In contrast, the sodiation process of TiS_2 is more complex. A recent review on the role of Ti in electrode materials for Na-ion batteries summarizes the recent studies for TiS_2.[11] As observed in the cyclic voltammetry of TiS_2 against Na, the two plateaus are observed and correspond to two different phase transitions of Na_xTiS_2; this feature implies a more sophisticated reaction between Na and TiS_2.[16, 17] Furthermore, the larger ion radius of Na^+ causes lower diffusivity and higher volume expansion of the host materials during insertion. This results in unfavorable kinetic reaction, potentially leading to some degradation of the performance.[17] As such, gaining a further quantitative understanding of the mechanism in the Na-TiS_2 system is vital to the advance of the technology and mitigation of the potential prominent issues.

In this work, we investigate the reaction mechanism of Na-TiS_2, and compare it with the Li-TiS_2 system,[1, 6, 18, 19] with an emphasis in providing quantitative, multi-modal analysis. To reveal the structural and chemical evolution of Na intercalation into TiS_2, the *operando* synchrotron-based X-ray absorption spectroscopy (XAS) and *ex situ* X-ray powder diffraction (XPD) measurements are employed. The number of chemical species involved in the reaction is determined by the

Multivariate Curve Resolution - Alternating Least Squares (MCR-ALS) method, applied to the *operando* X-ray Absorption Near Edge Structure (XANES) spectral data;[20] a character of the MCR-ALS method is that it determines the number of phases without pre-existing knowledge or assumption, and thus can be complementary to the XPD measurements. The modeling of *operando* Extended X-ray Absorption Fine Structure (EXAFS) spectra is used to resolve the local structural changes, quantifying the coordination numbers and interatomic distances of the structure during the electrochemical reactions and phase transformation; such analysis is important to understand the reaction mechanism and to correlate with the battery performance. To identify the intermediate phases during Na intercalation, Rietveld refinement in XPD, as a complimentary technique of XAS, is also conducted. By integrating all the information coherently together from combined theory and multi-modal synchrotron studies, this work provides a holistic understanding of the structural and chemical evolution of TiS_2, as well as contributing toward the methodological development.

2. Methods

2.1 Preparation of synchrotron *operando* cells and *ex situ* cells

The assembling of battery cells was conducted in an Ar-filled glovebox located in a humidity-controlled dry laboratory. In this work, an optically transparent tube cell as described previously[21], was used for synchrotron X-ray absorption spectroscopy (XAS) *operando* experiments as shown in Figure 1. The design of tube cell enables the direct observation on both anode and cathode sides, which can then be aligned to the X-ray beam at synchrotron beamlines. In our design, a Kapton (polyimide) tube was used as a cell body, with an inner diameter of 2.06 mm, a wall thickness of 25.4 μm. The current collectors are aluminum rod for the cathode, and stainless-steel rod for the anode. TiS_2 cathode slurry, which is composed of TiS_2(Sigma Aldrich): carbon black (Super C65, Imerys): polyvinylidene difluoride (PVDF, Alfa Aesar) = 30:15:5 by weight and mixed in N-Methyl-2-pyrrolidone (NMP, Sigma Aldrich), was directly coated onto the surface of the aluminum rod with a solid loading ~1.4 mg cm^{-2} and the anode is a small lithium or sodium cube ~1 mm^3 in size. During assembly, a layer of separator (Celgard 2325) was sandwiched between the cathode and anode to prevent shorting. The cell was then sealed by epoxy adhesive. The electrolyte used for Li cell was Lithium bis(trifluoromethane)sulfonimide (LiTFSI, 1.0 M) dissolved in 1,2-dimethoxyethane (DME) and 1,3-dioxolane (DOL) (1:1 by volume ratio). The electrolyte for Na was $NaClO_4$ (1.0 M). The total electrolyte was estimated to be 20 μL. The electrochemical performance of *operando* cell was conducted using a Biologic VSP-300 potentiostat.

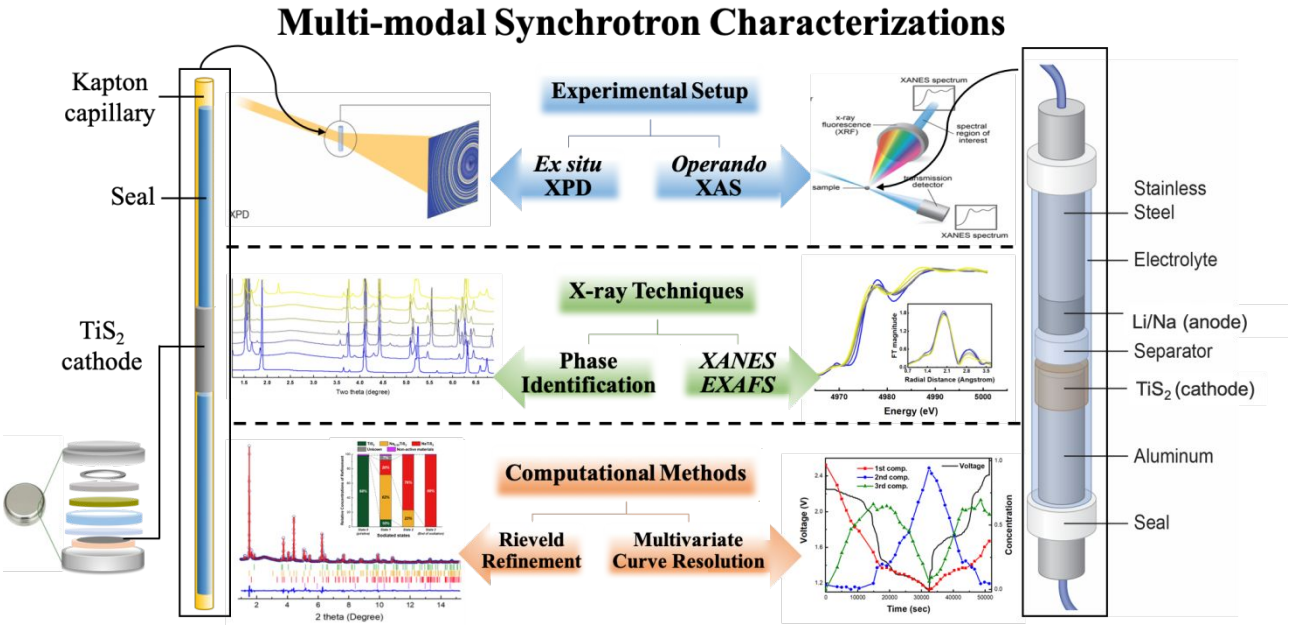

Figure 1. Schematic of the multi-modal synchrotron characterizations for the *operando* and *ex situ* experiments at various beamlines and the corresponding techniques/analysis applied.

In addition to *operando* tube cell, coin cell tests were carried out to confirm the consistency of reaction mechanism as compared to tube cell,[21] as well as to prepare the samples cycled to different state for *ex situ* XPD experiment. The TiS_2 cathode slurry, mixed with Super C65, PVDF, and NMP, were casted on a copper foil with a solid loading ~2.8 mg cm^{-2} using doctor blade with a thickness ~ 20 μm. Then, CR-2032 type coin cells were assembled following the sequence of TiS_2 cathode, glass fiber separator, Li/Na metal slice, stainless steel, and spring in a glove box. The electrolytes compositions were same as *operando* cells with the amount 60 μL. The assembled coin cells were tested using Arbin battery instrument. After cycled to various interested states, the assembled coin cells were opened in a glove box. The materials on cathode were collected and sealed in Kapton capillaries (inner diameter: 1 mm, wall thickness: 0.05 mm) for powder XRD experiment. Because of the difference of geometrical configuration, slow discharge/charge rates (≤C/10) were applied to both coin cells and *operando* cells to ensure the consistency of reaction mechanism.[21]

2.2 Synchrotron Characterizations

2.2.1. Hard-X-ray Absorption Spectroscopy

Operando X-ray Absorption Spectroscopy experiment of the Ti K-edge was conducted at the Inner-Shell Spectroscopy beamline (ISS, 8-ID), National Synchrotron Light Source-II (NSLS-II)

of Brookhaven National Laboratory (BNL). ISS beamline utilizes a damping wiggler source which provides a high flux (~ 5×10^{13} ph/s) and has an energy range from 4.9 keV to 36 keV with a 0.5 mm × 0.5 mm (h × v) spot size. Ti K-edge adsorption spectra could be acquired via tuning a cryogenically cooled double crystal Si(111) monochromator which enables energy fly-scanning mode. *Operando* spectra were recorded from the TiS_2 electrode in the fluorescence mode with a passivated implanted planar silicon (PIPS) detector. Scanning and data acquisition time was ~1 min per spectrum. Multiple cells were measurement consecutively as they undergo cycling. Data were collected every 8 minutes on each cell while the Li- or Na-TiS_2 battery was cycled at C/12 rate, a much slower rate than data acquisition rate. Three spectra were collected at each time point and averaged to further enhance data quality. With this measurement strategy, the collected spectra represented the chemical changes accurately with high quality. Adsorption spectra of Ti and TiS_2 (Sigma Aldrich) standard samples were collected in both transmission and fluorescence modes.

2.2.2. Tender Energy X-ray Absorption Spectroscopy

In addition to probing Ti, the experiment of *operando* X-ray Absorption Near Edge Structure (XANES) for sulfur (S) was conducted at the Tender Energy X-ray Absorption Spectroscopy (TES, 8-BM) beamline at NSLS-II. TES is optimized for spatially resolved XAS in the tender X-ray energy range, 2-5 keV, ideal for S K-edge analysis. TES employs a silicon (111) monochromator, and delivers a flux of approximately 10^{10} photons/s focused to an 8 μm × 45 μm (v × h) spot size by a set of Kirkpatrick-Baez mirrors.[22, 23] Sulfur absorption spectra were recorded in fluorescence mode using a solid-state Ge detector positioned perpendicular to beam direction. To reduce the attenuation of X-ray intensity at this energy, samples were contained within a Kapton tube and the sample chamber was helium-purged. Scanning and data acquisition time was ~ 0.5 min per spectrum, with 20 scans averaged per data point. Data were collected every 15 minutes on each cell. The Na-TiS_2 battery was cycled under a C/10 rate upon considering the data collection and beamline instrument session; this rate was slightly faster than the C/12 rate used at the ISS beamline but the battery displayed an identical electrochemical behavior. Absorption spectra of pure S and TiS_2 (Sigma Aldrich) standard samples were measured in fluorescence mode for energy calibration.

2.2.3. X-ray Powder Diffraction

The *ex situ* XPD experiment was conducted at the X-ray Powder Diffraction beamline (XPD, 28-ID-2) at NSLS-II.[24] To reduce effects of preferred orientation, the powders from the coin cells cycled to different states were removed from the current collector and sealed in Kapton capillaries;

each sample was measured at five different rotation angles relative to the X-ray beam. A large-area amorphous-silicon digital X-ray detector with 2048 × 2048 pixels, pixel size 200 × 200 μm, was used to collect the diffraction patterns. The sample to detector distance was first calibrated by using a Ni standard and determined to be 1566.37 mm. The X-ray beam size was 0.5 mm x 0.5 mm and the wavelength was 0.1877 A (X-ray energy was 66.05 keV). At this wavelength, the XPD beamline delivers a high intensity for resolving the weak peaks in the XRD patterns so that they can be used in the quantitative analysis. The exposure time of each scan was 30 seconds per 2D image.

2.3 Data analysis

2.3.1. X-ray Absorption Spectroscopy

The Demeter XAS Data Processing and Analysis software package was used to process the XAS data.[25] Normalization and background subtraction of the XAS spectra were conducted in Athena; linear regression was used to fit pre-edge region and a quadratic polynomial was regressed to fit the post-edge region. The Artemis software[25] with FEEF[26, 27] was used to conduct modeling in the EXAFS part of the data. The modeling provides the Ti-S and Ti-Ti coordination number and neighboring radial distance.

2.3.2. Multivariate Curve Resolution - Alternating Least Squares

Multivariate Curve Resolution-Alternating Least Squares (MCR-ALS) is commonly used method based on extracting meaningful information of the pure components in a mixture system through decomposition of data matrix D into the product of C and S^T matrices that contain pure profiles of components encoded as rows (usually concentrations) and columns (usually spectra), respectively.[28, 29] The model can be written as: $D = CS^T + E$ in which E is accounted for residuals not explained by resolved components. Given D as input matrix, the task of MCR-ALS is to find C and S matrices that minimize E based on user-defined constraints. In this work, we used the MCR-ALS MATLAB package provided by Jaumot *et al.*[30] and imposed non-negativity constraint on XANES spectrum and concentrations.[20] Equal height normalization of the XANES spectra prior to MCR-ALS decomposition did not yield any noticeable differences. 500 eV energy window of XAS (4900 to 5400 eV) was chosen as input for MCR-ALS. Tail of each pure component (μ(E) at 5400 eV) was used for normalization as post-processing.

2.3.3 XPD and Rietveld refinement

Each XPD pattern was integrated azimuthally and reduced to an intensity vs. 2θ (diffraction angle) plot. The peak locations were then compared with the standard references to identify the corresponding phases using commercial software package Jade (Materials Data, Inc.) and PDF-4+ 2018 (JCPDS-ICDD). After phase identification, the Rietveld refinements were conducted using TOPAS-Academic V6. Since all four samples contain multiple components, quantitative analysis was used to get weight percentage of each phase in each sample. The samples have slightly preferred orientation (PO) so a correction for the preferred orientation based on March's procedure[31] was applied in the refinement.

3. Results and Discussions

3.1. Electrochemical Characteristics

The representative discharge-charge curves of first cycle for *operando* cells working at synchrotron beamlines and conventional coin cells tested in laboratory are shown in Figure 2. The discharging cut-off voltage was selected to be 1.8 V for Li/TiS_2 and 1.1 V for Na/TiS_2 while the charging cut-off voltage for both cases is 2.6 V. Since the *operando* cells have a different geometrical configuration from coin cell, the kinetics and actual capacity could deviate from the reaction in coin cell. As shown in Figure 1, the design of *operando* cell introduced a longer distance (2~6 mm) from anode to cathode, asymmetrical electrodes in shape, and an uncertainty of electrode weight.[21] These factors would make the reaction to reach equilibrium with a longer time and more challenging to define the exact states when comparing *operando* cell and coin cell. As a result, the x-axis of relative capacity in Figure 2 was not normalized by the theoretical capacity value. Instead, the relative capacity was normalized by the capacity value at the fully reacted state. In this way, the difference of the geometrical configuration between *operando* cell and coin cell could be minimized. The chemical states of the two types of cell could then be compared. Hence, after normalization, the observed electrochemical profiles of Li-TiS_2 and Na-TiS_2 in *operando* cells agree well with the profiles in coin cell as well as the previous reports.[3, 16, 32]

The smooth electrochemical profiles in lithiation and de-lithiation processes indicate a single-phase reaction. The space groups before lithiation (TiS_2) and after lithiation ($LiTiS_2$) are all known as $P\bar{3}m1$.[17] The discharging/charging reaction of Li/TiS_2 only involves the intercalation/de-intercalation of Li ions inserting into and extracting from the space between TiS_2 layers, which leads to an increase of the lattice parameters. On the other hand, the multi-plateau electrochemical curves in sodiation and de-sodiation, as shown in Figure 2, imply likely crystal space group

symmetry change, which involves the formation of undetermined intermediate phases[12, 33] in addition to the fully sodiated product, $NaTiS_2$, whose stable space group is predicted to be $R\bar{3}m$.[17] To understand the structural and chemical evolution of TiS_2 in these two systems – Li ions and Na ions batteries – their *operando* XAS and *ex situ* XPD characterizations will be discussed below.

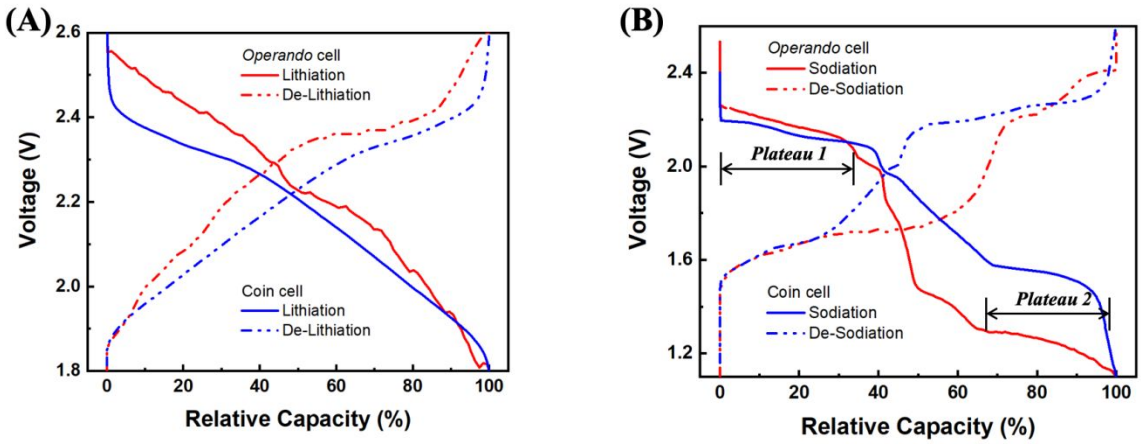

Figure 2. The electrochemical profiles of *operando* cell (red lines) compared with coin cell (blue lines) for lithiation/de-lithiation in (A) and sodiation/de-sodiation in (B).

3.2. Chemical Evolution by X-ray Absorption Spectroscopy at Ti and S K-edges

In order to study the states of structural and chemical changes during battery reaction, a series of *operando* XAS experiments of TiS_2 against Li and against Na were conducted through two synchrotron X-ray beamlines: ISS and TES at NSLS II, BNL. The Ti K-edge (4966 eV) XANES was conducted at ISS beamline, while the S K-edge (2472 eV) XANES was conducted at TES beamline, for their complementary nature.

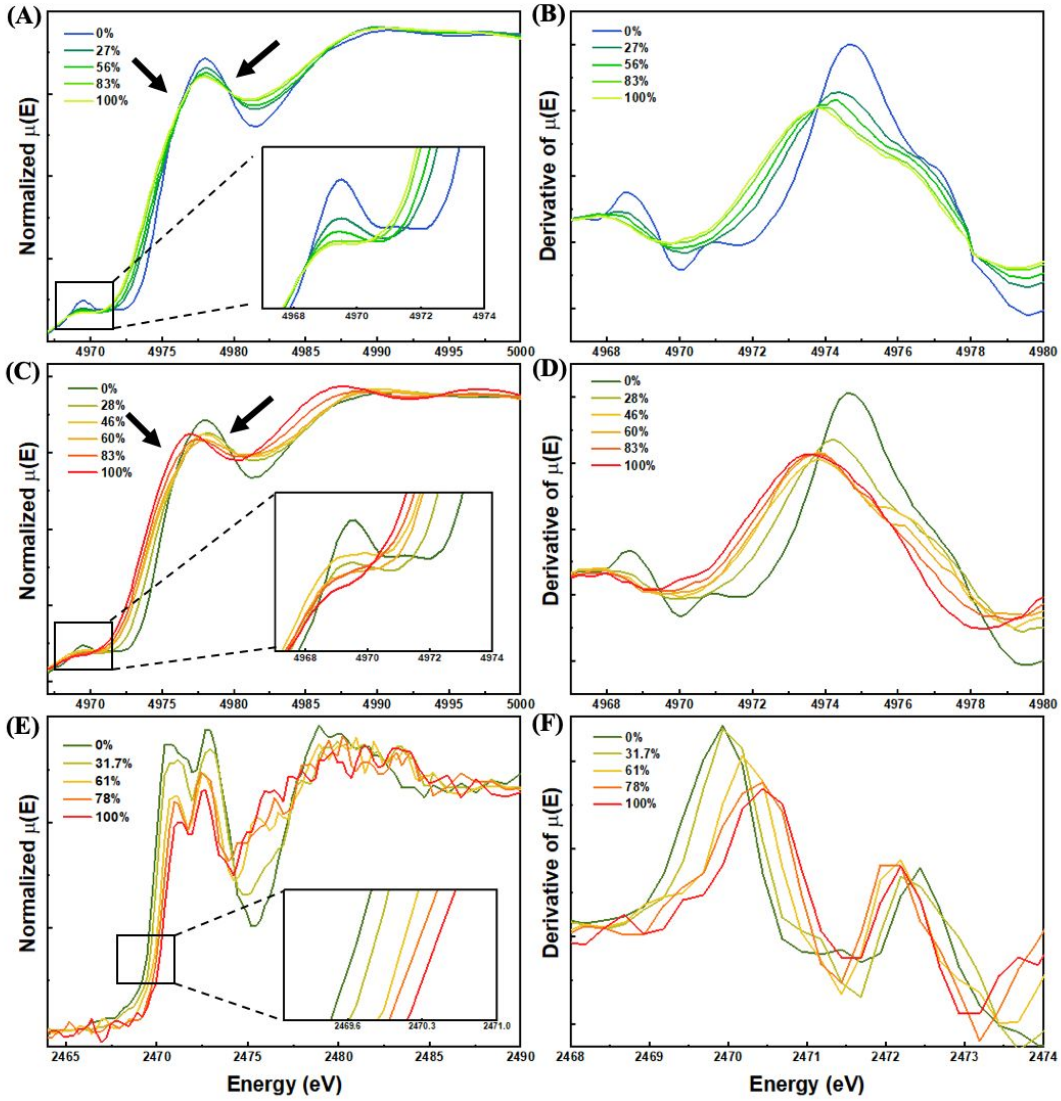

Figure 3. The *operando* XANES spectra in the first cycle and its corresponding first derivatives. (A, B) Ti K-edge for the lithiation process, (C, D) Ti K-edge for the sodiation process, (E, F) S K-edge for the sodiation process with X-ray attenuation relative to the incident X-ray energy. Insets show the details of the pre-edge features.

Figure 3 shows the *operando* XANES spectra measured at TiS_2 electrode as a function of different depth of discharge. For both lithiation and sodiation processes in TiS_2, the Ti K-edge positions shift towards lower energy as shown in Figure 3(B) and (D) by observing the main peaks moving to a lower energy in the first derivative of the X-ray attenuation relative to the incident X-ray energy. The shifts toward the lower energy imply that Ti ions of TiS_2 was reduced during discharge

where Ti acted as an electron acceptor during the insertion of alkali ions. Meanwhile, the pre-edge peaks whose details are shown in the insets of Figure 3(A) and (C) become less prominent as the Li or Na intercalates into TiS_2 layers. These pre-edge peaks are attributed to transitions from Ti-1s orbital to the Ti-3d/S-3p hybrid orbital in a partially distorted octahedral strucuture.[19, 34, 35] Previous studies have indicated that the decreasing intensity at pre-edge of Ti in lithiation could be related to the repulsive interaction of inserted Li ions and Ti ions in TiS_2.[19, 35] The insertion may symmetrize the distorted octahedral environment of Ti atoms to suppress the pre-edge peak,[19, 35] while expanding the lattice spacing. We observe similar Ti pre-edge suppression during sodiation.

However, besides shifts in the main edge and the decrease of the pre-edge peak intensity, the main edge of XANES spectra in sodiation evolve distinctively once the sodiation reaction exceeds 60% of capacity, as labeled with an arrow in Figure 3(C). The spectra exceeded 60% of capacity did not cross each other and led to the elimination of the isosbestic point. Such clear spectra's shape change did not occur in the lithiation case as shown in Figure 3(A), where the symmetry group of TiS_2 and Li_xTiS_2 remains unchanged during discharge. Appearance of an isosbestic point in a spectral series is an evidence for a simple A-to-B transformation. It could be chemical state change or phase transformation but as long as only two states are involved. These new XANES spectral features in sodiation of TiS_2 thus indicate that instead of a simple A-to-B transformation, there is an intermediate involved in the sodiation process.[33] Further quantification analysis needs to be carried out to predict the unknown reaction products of sodiation which correspond to the multi-plateau electrochemical profile as observed in the sodiation of TiS_2.

The *operando* XANES spectra of S K-edge and their first derivatives during sodiation are shown in Figure 3(E) and (F). From the spectra, the edge positions of S shift to higher energy during sodiation. This result is consistent with the analysis of density of states done by Zhang *et al.*[19] In their report, the electrons transfer from Li ions not only to titanium but also to sulfur during intercalation as well as conversion reaction. This may imply that sulfur also involves in the sodiation reaction and receive electrons. The slightly noisy data observed in the TES S-edge XANES may be attributed to the challenge in obtaining data in *operando* cells with high signal-to-noise ratio at the tender X-ray range; however, it is sufficient to provide information regarding the battery reaction evolution.

Although the change of oxidation state and geometrical symmetry in the lithiation and sodiation reactions could be extracted from the *operando* XANES spectra, identifying the number and the nature of the chemical components involved in the sodiaiton process required further analysis. Multivariate Curve Resolution - Alternating Least Squares (MCR-ALS) method[36] was applied to the *operando* XANES data sets to unravel pure spectral components. In MCR-ALS method, the number of pure components is a user-defined variable. Evolving Factor Analysis (EFA)[37, 38] is a commonly used method to estimate the number of pure components. Figure S1(A-B) showed the EFA calculation for lithiation and sodiation XANES spectra. Although first two factors are

emergent, higher order factors are not easily distinguishable from the noise level. Therefore, we varied and tested the number of pure components between 2 and 8. The χ^2 values of the Pearson correlation coefficient (goodness of fit) versus the number of pure components in deconvolution are also shown in Figure S1(C); note that this goodness of fit value does not improve significantly after 3 components. The calculated spectra of pure components for both lithiation and sodiation processes using 2-4 components are shown in Figure S1(D-I). In both lithiation and sodiation cases, the deviation of calculated spectra from experimental spectra decreases as the number of components increases; this trend is statistically expected when calculating the goodness of fit. For lithiation, it is well-understood that the intercalation of Li in TiS_2 does not cause any phase transformation; i.e., TiS_2 and $LiTiS_2$ share the same space group and only the expansion of lattice parameters occurs.[3, 18] Therefore, the lithiation process is known to be a single-phase and two-component reaction. This is consistent with the present MCR-ALS analysis. The third component from the deconvolution resembles the second component, suggesting that two pure components are sufficient to describe the phase transformation. In comparison, the presence of a third component with distinct XANES features is evident in the MCR-ALS results for sodiation. Two-component solution for the lithiation spectra reproduces experimentally known phases. On the other hand, second and third components are almost identical in three-component case, as shown in Figure S1(E). For the case of sodiation, goodness of fit significantly improves upon inclusion of third component. However, inclusion of fourth component produces unrealistic XANES spectra as shown in the revised Figure S1(F&I). The final deconvoluted pure-component spectra for the lithiation and sodiation processes are shown in Figure 4(A) and (B), with two and three components respectively.

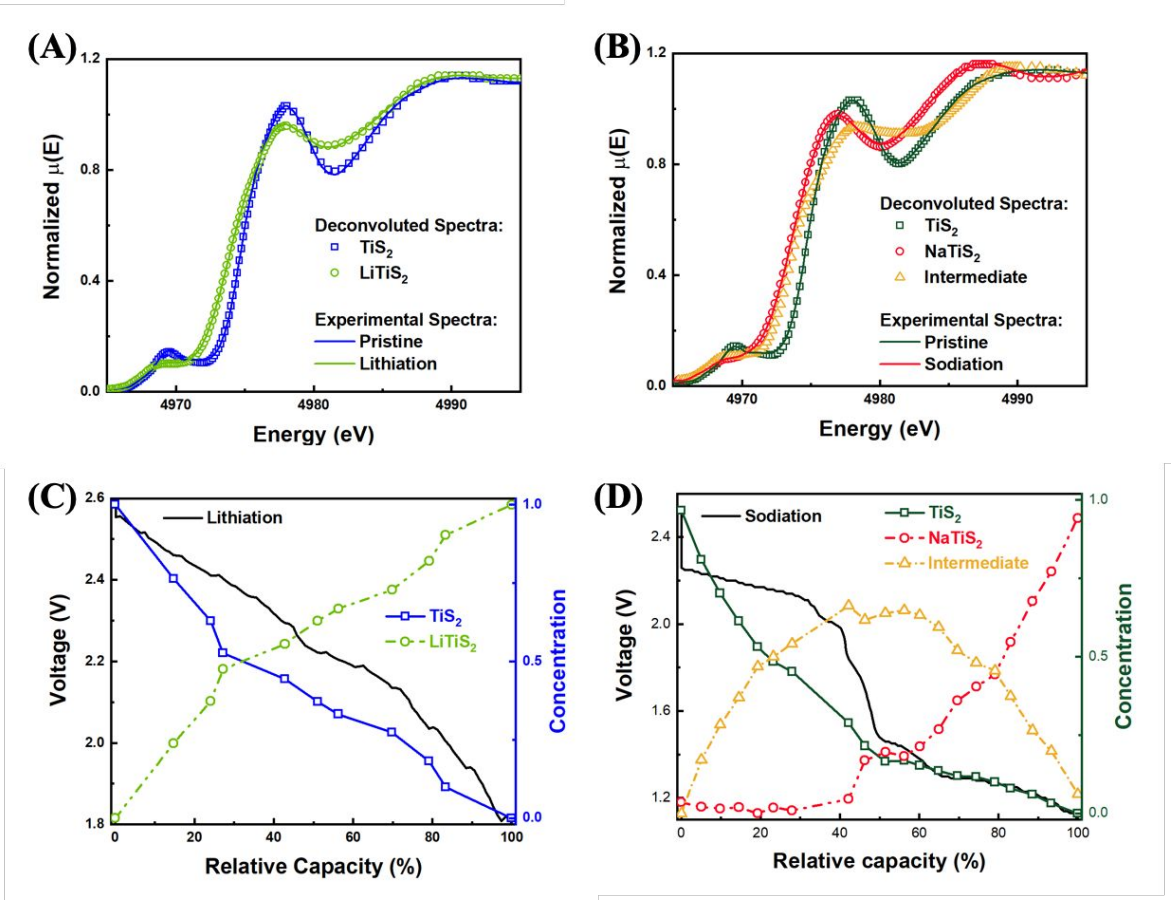

Figure 4. MCR-ALS analysis of *operando* XANES series: Deconvoluted pure components for lithium (A) and sodium (B). Concentration evolutions of two-component and three-component reaction for lithium (C) and sodium (D) respectively.

The concentration evolution of the two-component reaction for lithiation is shown in Figure 4(C) and the three-component sodiation reaction in Figure 4(D). As seen in Figure 4(C), the lithiation process starts with the 1st component, whose concentration gradually reduces, while the end-product corresponding to 2nd component gradually increases in concentration till the end of the lithiation. The starting phase (i.e. the 1st component) from spectral deconvolution is thus identified as pristine phase TiS_2, whereas the 2nd component is identified as the lithiated Li_xTiS_2 phase.

In comparison, the sodiation process is shown in Figure 4(D). Similar to the lithiation process, the decrease of the 1st component from the start of the sodiation and the appearance of the 2nd component during the sodiation were observed, where the 1st component is identified as TiS_2 and the 2nd component as the fully sodiated $NaTiS_2$. Interestingly, an additional phase, 3rd component, appears during the sodiation reaction and reaches its maximum at the capacity of about 50%. Furthermore, the main edge positions from the 1st component (pristine TiS_2), to the 3rd component (additional phase), and finally to the 2nd component (end product of sodiation), displays a shift

toward lower energy; this shift is consistent with the experimental spectra as shown previously in Figure 3(D). These results indicate that the 3rd component is an intermediate product which is introduced during sodiation but diminishes at the end of sodiation.

3.3. Phase Identification and Refinement by X-ray Powder Diffraction

To determine the intermediate phase of sodiation, shown as the 3rd component in the MCR-ALS analysis of XANES in the previous section, we conducted XPD measurements on samples at different states of charge and carried out Rietveld refinement on these XPD patterns. The electrochemical data for the *ex situ* XPD samples are included in Figure S4, with each state labeled. The chemical species with different long-range orders are identified at various discharging depth in Figure 5(A) while their corresponding relative concentrations are calculated from refinements and summarized in Figure 6.

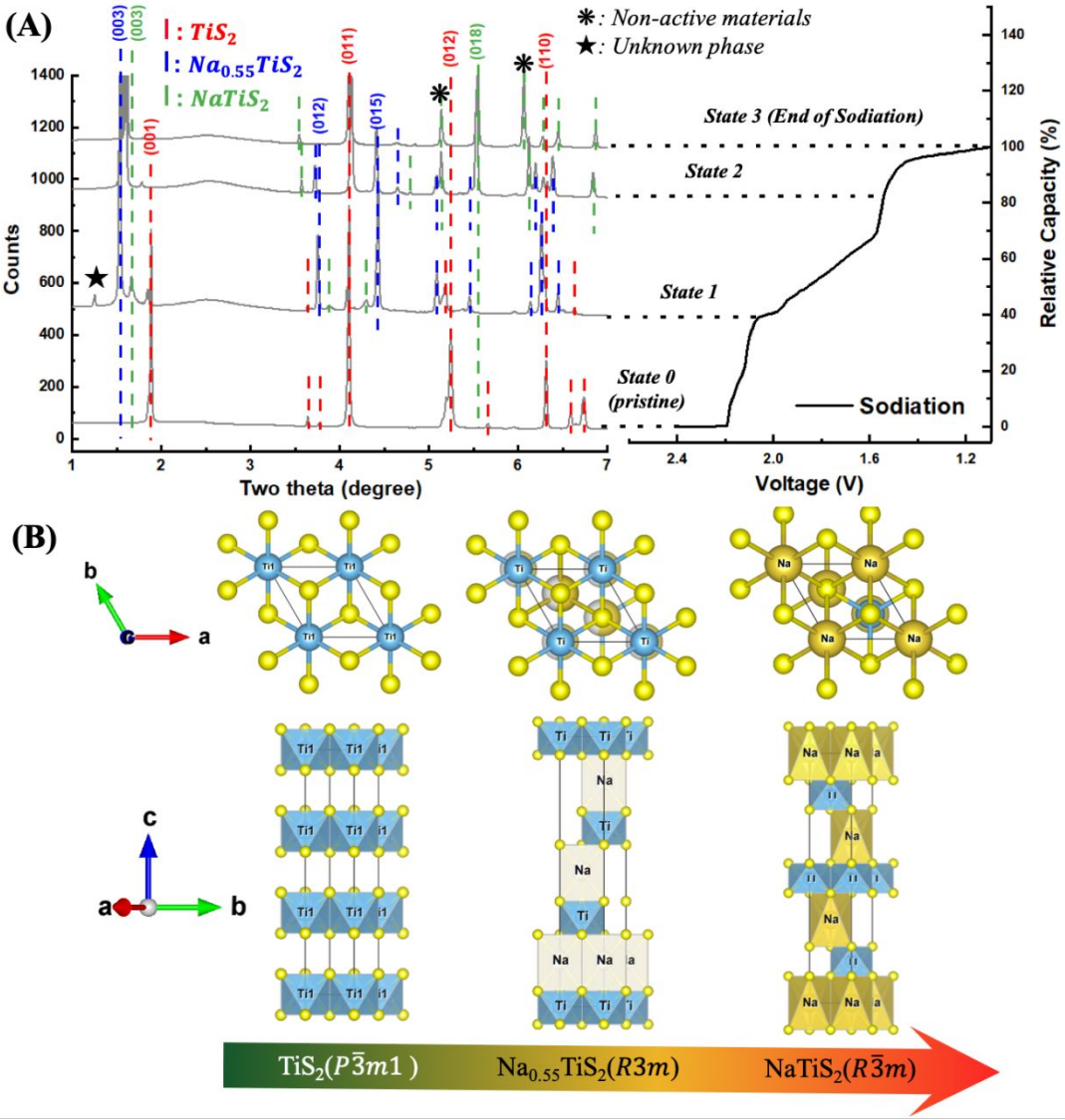

Figure 5. (A)The *ex situ* XPD patterns from the TiS_2 electrode aligned with its corresponding electrochemical profile during sodiation. The peaks from non-active materials including the current collector are marked with (✱). (B)The major crystal structures involved in sodiation at each cycled state.[39]

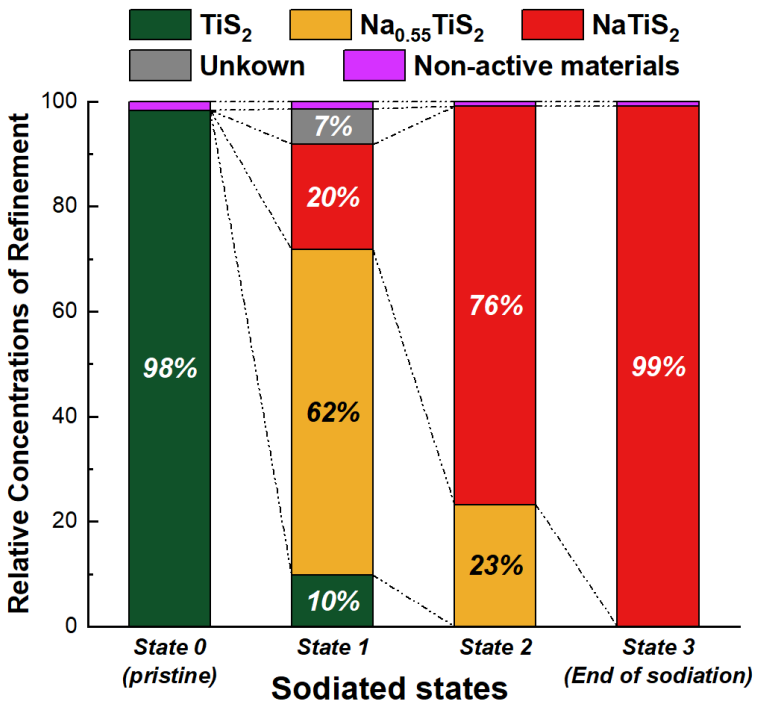

Figure 6. The relative concentrations (%) calculated by Rietveld refinement at different discharging states as labeled in Figure 5(A). The unknown phase is assumed to be $Na_{0.3}TiS_2$ in the quantitative phase analysis.

The refinement profiles in Figure S2 and the fitting parameters in Table S1 confirm that three phases, TiS_2, $Na_{0.55}TiS_2$, and $NaTiS_2$, are involved in the sodiation reaction.[31, 40] As the pristine TiS_2 is sodiated to *State 1*, the system evolves into a three-component mixture where $Na_{0.55}TiS_2$ is the main component. As the sodiation process moves to *State 2*, TiS_2 has fully transformed into $Na_{0.55}TiS_2$ and $NaTiS_2$, with $NaTiS_2$ becoming dominant. Finally, the system turns into a pure phase of $NaTiS_2$ at the end of the sodiation.

The intensity variation of the diffraction peaks, e.g., TiS_2 (001) peak, as well as $Na_{0.55}TiS_2$ (003) and $NaTiS_2$ (003), is shown in Figure 5(A). At *State 1*, the strongest peak is $Na_{0.55}TiS_2$ (003) which has the largest *c-axis* lattice parameter. However, the *c-axis* length becomes shorter as diffraction peaks shift to higher diffraction angles during further sodiation. This is because the space group of $Na_{0.55}TiS_2$ is $R3m$ while the space group of $NaTiS_2$ is $R\bar{3}m$. When a Na atom is inserting into TiS_2 layers, it will stack on top of a Ti atom to form $Na_{0.55}TiS_2$ first. As more Na ions are driven into TiS_2, an offset along the *a-b plane* happens so that the stacked Na atoms are no longer directly on top of Ti atoms; the system prefers this offset to reduce the lattice expansion and to stabilize the crystal structure. This offset makes the *c-axis* parameter of $NaTiS_2$ smaller than $Na_{0.55}TiS_2$, as

illustrated in Figure 5(B). The presence of three phases during the sodiation of TiS_2 is consistent with the calculated phase diagram of Na_xTiS_2 that shows O1, P3 and O3 stacking of TiS_2 layers.[41] Nevertheless, there is still an unknown phase at *State 1*. A $P\bar{3}m1$ structure $NaTi_3S_6$ with $c = 25.83$ Å, which is isostructural to the lithium counterpart, may be adopted to fit the peaks of this "unknown phase"; note that $NaTi_3S_6$ is not a measured structure in database where lattice parameters are confirmed by experiment. The structure and lattice parameters of $NaTi_3S_6$ are calculated and believed to be a metastable phase in the sodiation of TiS_2. Overall, this unknown phase contributes ~7% to the all the crystalline phases detected. Since the model accounts for only 3 weak peaks in the XPD patterns, and is not a known structure in existing structure data bases, we cannot confirm its structure with our XPD data. Some reports indicate the observation of certain intermediate phases, $Na_{0.22}TiS_2$[12, 14] and $Na_{0.25}TiS_2$,[15] but the lattice parameters are inconsistent with the XPD results shown here. Recently, *Wang et al* reported the investigation of sodiation process in TiS_2 nanoflakes by *in situ* transmission electron microscopy.[42] They predicted the formation of $Na_{0.33}TiS_2$ phase and confirmed it as a thermodynamic preferred phase by first-principles calculations where is very consistent to our hypothesis of the unknown phase in Figure 5(A). Overall, this unknown phase could be a metastable Na_xTiS_2 phase with $x < 1/3$.

The supplementary information includes a summary of quantification results of MCR-ALS and Rietveld refinements based on relative capacity (Table S2) and absolute capacity (Table S3). These two analyses show agreement regarding the general trend, and yet differ in the quantitative details as discussed in the supplementary information. These discrepancies represent the conditions in multimodal characterization, as well as comparing the *operando* and *ex situ* studies. XRD detects long-range ordered, crystalline structures while XAS not only measures ordered phases but also is sensitive to non-crystalline and highly disordered materials. *Operando* studies generally require modification on the battery cells and measurement is performed when materials are under non-equilibrium states during reactions; in contrast, the samples measured under *ex situ* or post-cycled analysis can be generally measured under ideal technical conditions and yet not while the reactions are taking place. While comparing the results quantitatively depends on the experimental conditions, the results show that both *operando* and *ex situ* across multiple characterization techniques can be used together to provide complementary information for a more complete analysis.

3.4. Atomic Structure Modeling using Extended X-ray Absorption Fine Structure (EXAFS)

The above discussions show a quantitative analysis of the chemical and structural revolutions of TiS_2 in lithiation and sodiation based on the *operando* XANES and *ex situ* XPD studies. To further understand the local chemical and structural changes, we created atomic model to fit the Extended X-ray Absorption Fine Structure (EXAFS) region in the Ti XAS data. The key fitting parameters include the coordination number and interatomic distance for Ti-S (first shell) and Ti-Ti (second shell) of TiS_2. Figure 7(A) and (B) show the radial distribution function of the EXAFS spectra in

operando XAS experiments during lithiation and sodiation at various reaction depths, obtained by calculating the Fourier Transformation (FT) of the EXAFS spectra. The corresponding k^2 -weighted EXAFS $\chi(k)$ spectra and the FT window are shown in Figure S6.

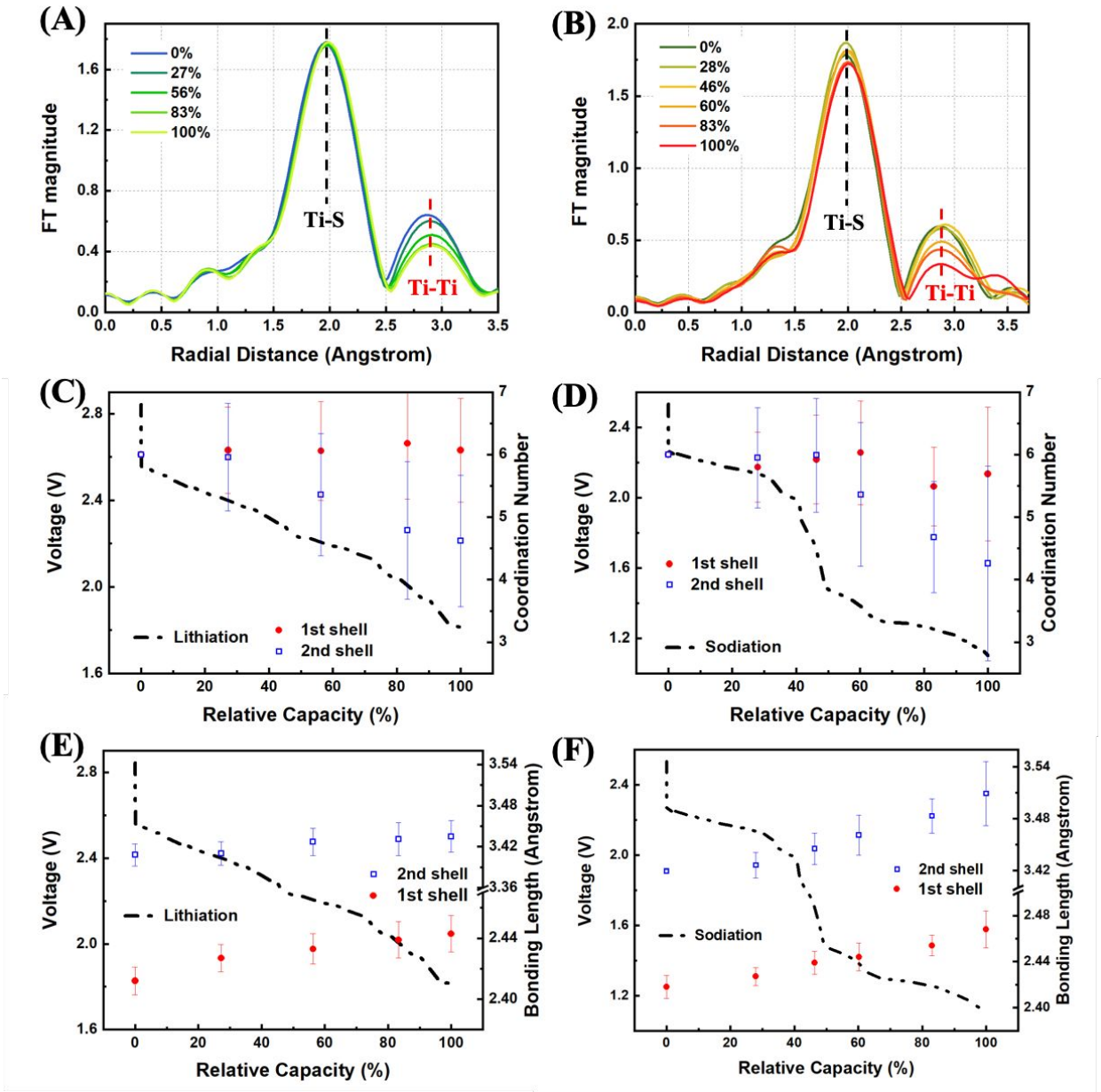

Figure 7. The radial distribution functions of EXAFS part in *operando* XAS experiments during (A) lithiation and (B) sodiaiton at the various discharging states. The modeling results of EXAFS spectra on Ti-S (1st shell) and Ti-Ti (2nd shell): (C-D) Coordination number and (E-F) bonding length evolutions in both lithiation and sodiation.

The intensity of the second-shell (Ti-Ti) in the radial distribution functions decrease in both lithiation and sodiation reactions. This observation is consistent with the EXAFS fitting results shown in Figure 7(C) and (D). During lithiation, the number of S atoms surrounding Ti core atom has little change from 6 to 5.77 while the coordination number of Ti-Ti (second shell) decreases from 6 to 4.67. Similarly, during sodiation, the number of neighboring S atoms around Ti changes only from 6 to 5.69 whereas the coordination number of Ti-Ti reduces from 6 to 4.26. This implies that the insertion of Li or Na ions results in a local structural change of TiS_2 on Ti-Ti shell, which may cause the formation of sub-layer TiS_2 with less neighboring Ti around Ti core atoms, making the layers discontinuous.

The distributions of bond length in Ti-S and Ti-Ti shells for lithiation and sodiation are displayed in Figure 7(E) and (F) respectively. The bonding length of both the first shell (Ti-S) and second shell (Ti-Ti) elongates during both lithiation and sodiation reactions. The increasing interatomic distance of Ti-S and Ti-Ti indicates that the two reactions not only open the space between TiS_2 layers but also increase the space on the *a-b* plane perpendicular to *c-axis* direction. Compared to the crystal structure derived from XPD, the results of expansion on *a-b plane* from EXAFS in lithiation and sodiation are quantitatively consistent with the lattice parameters calculated from XPD results, as shown in Table 1.

In addition, several works reported that there is a decay in Coulombic efficiency after the first cycle of the Li-TiS_2[6, 19] and Na-TiS_2.[12, 33] In Figure S5, electrochemical cycling tests of Li-TiS_2 and Na-TiS_2 coin cells reacted at 0.1C rate are provided. This decay is usually attributed to the formation of the solid electrolyte interphase (SEI) in lithiation case.[6, 19] The formation of SEI would permanently consume part of active materials and thus lead to the fading of specific capacity in batteries. As a result, how much the active materials get reversible after the first cycle is another important issue for the application of Li/Na-TiS_2 batteries. Thus, the modeling of the EXAFS spectra during de-lithiation and de-sodiation are carried out as shown in Figure S3. For both processes, the Ti-Ti coordination number and bonding length of 1st & 2nd shells were found to be close to those of TiS_2 state. However, the de-lithiation and de-sodiation do not recover the pure TiS_2 phase. As summarized in Table 1, in the case of Li-TiS_2 battery, the bond lengths recover within 0.01A whereas the Ti-Ti coordination number changes from 6 to 5.26. By contrast, in the case of Na-TiS_2 battery, the Ti-Ti coordination number is fully restored but Ti-Ti bond length increases, indicating a larger lattice expansion. The incomplete reactions in both de-lithiation and de-sodiation agree with the decay of Coulombic efficiency after the first cycle, but the mechanism behind this decay differs between Li and Na.

Table 1. The refined structural parameters for TiS_2 electrodes obtained from *operando* XAS data at the end states of battery reaction; the parameters of *a-axis* which equals to Ti-Ti bond derived from XPD are included for comparison.

Parameters		Pristine TiS_2	Full Lithiation	Full De-lithiation	Full Sodiation	Full De-sodiation
Coordination Number	Ti-S	6	6.07 ± 0.83	6.14 ± 0.78	5.69 ± 1.07	5.70 ± 0.68
	Ti-Ti	6	4.62 ± 1.05	5.26 ± 0.92	4.26 ± 1.56	5.98 ± 1.00
Bond Length (Å)	Ti-S	2.430	2.44 ± 0.01	2.42 ± 0.01	2.47 ± 0.02	2.44 ± 0.01
	Ti-Ti	3.410	3.44 ± 0.02	3.41 ± 0.02	3.51 ± 0.04	3.44 ± 0.02
a-axis from XPD (Å)		3.41	3.42		3.55	

4. Conclusion

This work provides further mechanistic insights into alkali metals insertion in layered transition metal dichalcogenides during battery charge and discharge. By applying a combination of *operando* X-ray absorption spectroscopy, multivariate curve resolution analysis, and *ex situ* X-ray powder diffraction, we investigated the chemical and structural evolutions of TiS_2 during sodiation in order to understand the reaction mechanism of TiS_2 in Na-ion batteries. From XANES spectra, the edge shifts toward lower energy indicate that Ti ions are reduced in both the lithiation and sodiation reactions. Simultaneously, sulfur also participates in the redox reaction in sodiation.

The XANES spectral shape variations, e.g. isosbestic points, imply that the lithiation is a pure intercalation reaction, whereas sodiation involves a more complex structural change. Via the MCR-ALS analysis, the calculations identified chemical components that participate in lithiation and sodiation. The deconvoluted spectra showed that the lithiation and sodiation processes are two- and three-component reactions respectively. The third component in the sodiation is an intermediate phase.

The three components involved in the Na-TiS_2 reaction are found to be a conversion process from TiS_2 to $Na_{0.55}TiS_2$, and finally to $NaTiS_2$ using XPD experiments and Rietveld refinements. During sodiation, the *c-axis* length starts to increase when TiS_2 ($3c = 17.1$ Å) transforms into $Na_{0.55}TiS_2$ ($c = 20.94$ Å) but then decreases when $Na_{0.55}TiS_2$ becomes $NaTiS_2$ ($c = 20.58$ Å). The c parameter in TiS_2 is tripled since it has only one MO_6 octahedral layer in its unit cell, whereas Na_xTiS_2 phases have three. Overall the crystal structure changes from $Na_{0.55}TiS_2$ ($R3m$) to $NaTiS_2$ ($R\bar{3}m$) and leads to an *a-b plane* offset to 'unstack' the Na atoms from the Ti atoms and a shrinkage of the *c-axis*, thereby stabilizing the structure. The main reason led to the different intercalation mechanism is believed to be the larger size of Na ion than Li ion.

From the EXAFS modeling, the structural evolution in lithiation/de-lithiation and sodiation/de-sodiation causes different impacts on the decay of the Columbic efficiency after cycling. The

increasing interatomic distances of Ti-S and Ti-Ti shells in both lithiation and sodiation reactions show that the intercalation of Li and Na atoms not only leads to *c-axis* expansion but also to a lattice space opening along the *a-b plane*. The decreasing coordination numbers of the Ti-Ti shell may indicate the local structural change to form TiS_2 sub-layers. However, the incomplete recovery of Ti-Ti coordination number in de-lithiation implies some degree of breakdown of the structure; this results in a known degree of decay of coulombic efficiency.[6, 12] In contrast, sodiation involves structural change including shifts in stacking of layers; this rearrangement leads to an incomplete recovery of the *c* lattice parameter, but better recovery of Ti-Ti coordination number. This mechanism may explain why Na-TiS_2 has a better restoration of active materials, by re-structuring after every cycle, and potentially better lifetime efficiency than Li. The different structural recoveries among de-lithiation and de-sodiation may explain why Li-TiS_2 and Na-TiS_2 have different cycling performances, but further work is required to understand this structure-performance correlation. Analysis combining EXAFS, diffraction and other techniques to analyze the structural changes in multiple cycles, for both crystalline and amorphous phases, would be invaluable. The studies to fully understand the mechanism of TiS_2 would enhance the design of optimal TiS_2 matrix for Li and Na on various purposes, e.g. Li-TiS_2 for fast rate and small-scale application and Na-TiS_2 for slow rate but large-scale energy storage.

Author Contributions

K Sun, H Gan, and Y-cK Chen-Wiegart developed the initial research concept, with further discussion on multimodal data analysis with E Stavitski and D Yu. Y-cK Chen-Wiegart wrote the synchrotron beamtime proposals with the input from H Gan and K Sun to obtain instrument time. K Sun designed the *operando* cells. C-H Lin assembled the cells and performed the electrochemical measurements. E Stavitski designed, commissioned and setup ISS beamline. P Northrup designed, commissioned and setup TES beamline. C-H Lin, C Zhao, and Y-cK Chen-Wiegart conducted the synchrotron XAS experiments with E Stavitski at ISS and with P Northrup at TES. C-H Lin performed the XAS data analysis under the supervision of E Stavitski and Y-cK Chen-Wiegart. M Topsakal conducted the MCR-ALS analysis under the supervision of D Yu. C-H Lin and C Zhao disassembled the *ex situ* cells and prepared powder samples for XPD experiments. C-H Lin, C Zhao and Y-cK Chen-Wiegart conducted the synchrotron XPD experiments with J Bai and E Dooryhee. C-H Lin analyzed the XPD data under the guidance of J Bai. J Bai conducted the Rietveld refinement. C-H Lin, M Topsakal, K Sun, J Bai, H Gan, D Lu, E Stavitski and Y-cK Chen-Wiegart interpreted the data. C-H Lin wrote the manuscript under the supervision of Y-cK Chen-Wiegart, with the inputs from all co-authors.

Conflicts of interest

There are no conflicts to declare

Acknowledgements

This work is supported by the U.S. Department of Energy (DOE) Office of Energy Efficiency and Renewable Energy under the Advanced Battery Materials Research (BMR) program, Contract No. DE-SC0012704. This research used resources 8-ID (ISS), 8-BM (TES) and 28-ID-2 (XPD) beamlines of the National Synchrotron Light Source II, a U.S. DOE Office of Science User Facility operated for the DOE Office of Science by Brookhaven National Laboratory under Contract No. DE-SC0012704. We acknowledge Dr. Klaus Attenkofer for his support during ISS beamtime. K. Chen-Wiegart and C-H Lin acknowledge the support by the Department of Materials Science and Chemical Engineering, the College of Engineering and Applied Sciences, and the Stony Brook University, as well as by the Center for Functional Nanomaterials, which is a U.S. DOE Office of Science Facility, at Brookhaven National Laboratory under Contract No. DE-SC0012704.

References

1. E. A. Suslov, O. V. Bushkova, E. A. Sherstobitova, O. G. Reznitskikh and A. N. Titov, *Ionics*, 2016, **22**, 503-514.
2. G. B. Haxel, J. B. Hedrick and G. J. Orris, *U.S. Geological Survey*, 2002, USGS Fact Sheet 087-002.
3. M. S. Whittingham, *Science*, 1976, **192**, 1126-1127.
4. A. H. Thompson, *Phys. Rev. Lett.*, 1975, **35**, 1786-1789.
5. S. N. Li, J. B. Liu and B. X. Liu, *Journal of Power Sources*, 2016, **320**, 322-331.
6. A. Chaturvedi, P. Hu, V. Aravindan, C. Kloc and S. Madhavi, *J Mater Chem A*, 2017, **5**, 9177-9181.
7. B. B. Tian, W. Tang, K. Leng, Z. X. Chen, S. J. R. Tan, C. X. Peng, G. H. Ning, W. Fu, C. L. Su, G. Y. W. Zheng and K. P. Loh, *ACS Energy Lett.*, 2017, **2**, 1835-1840.
8. K. Sun, Q. Zhang, D. C. Bock, X. Tong, D. Su, A. C. Marschilok, K. J. Takeuchi, E. S. Takeuchi and H. Gan, *Journal of the Electrochemical Society*, 2017, **164**, A1291-A1297.
9. M. D. Slater, D. Kim, E. Lee and C. S. Johnson, *Advanced Functional Materials*, 2013, **23**, 947-958.
10. N. Yabuuchi, K. Kubota, M. Dahbi and S. Komaba, *Chem Rev*, 2014, **114**, 11636-11682.
11. Y. S. Wang, W. Zhu, A. G. Fi, C. Kim and K. Zaghib, *Front. Energy Res.*, 2019, **7**, 12.
12. Y. P. Liu, H. T. Wang, L. Cheng, N. Han, F. P. Zhao, P. R. Li, C. H. Jin and Y. G. Li, *Nano Energy*, 2016, **20**, 168-175.
13. A. Chaturvedi, E. Edison, N. Arun, P. Hu, C. Kloc, V. Aravindan and S. Madhavi, *ChemistrySelect*, 2018, **3**, 524-528.
14. H. W. Tao, M. Zhou, R. X. Wang, K. L. Wang, S. J. Cheng and K. Jiang, *Adv. Sci.*, 2018, **5**, 7.
15. B. Han, S. L. Chen, J. Zou, R. W. Shao, Z. P. Dou, C. Yang, X. M. Ma, J. Lu, K. H. Liu, D. P. Yu, L. P. Wang, H. C. Wang and P. Gao, *Nanoscale*, 2019, **11**, 7474-7480.
16. G. H. Newman and L. P. Klemann, *Journal of the Electrochemical Society*, 1980, **127**, 2097-2099.
17. S. P. Ong, V. L. Chevrier, G. Hautier, A. Jain, C. Moore, S. Kim, X. H. Ma and G. Ceder, *Energy & Environmental Science*, 2011, **4**, 3680-3688.
18. Q. Zhang, D. C. Bock, K. J. Takeuchi, A. C. Marschilok and E. S. Takeuchi, *Journal of the Electrochemical Society*, 2017, **164**, A897-A901.
19. L. Zhang, D. Sun, J. Kang, H. T. Wang, S. H. Hsieh, W. F. Pong, H. A. Bechtel, J. Feng, L. W. Wang, E. J. Cairns and J. H. Guo, *Nano Lett.*, 2018, **18**, 4506-4515.
20. P. Conti, S. Zamponi, M. Giorgetti, M. Berrettoni and W. H. Smyrl, *Anal. Chem.*, 2010, **82**, 3629-3635.
21. K. Sun, C. H. Zhao, C. H. Lin, E. Stavitski, G. J. Williams, J. M. Bai, E. Dooryhee, K. Attenkofer, J. Thieme, Y. C. K. Chen-Wiegart and H. Gan, *Sci Rep*, 2017, **7**, 10.
22. P. Northrup, A. Leri and R. Tappero, *Protein Pept. Lett.*, 2016, **23**, 300-308.
23. P. Northrup, *J. Synchrot. Radiat.*, 2019, **26**, 2064-2074.
24. X. B. Shi, S. Ghose and E. Dooryhee, *J. Synchrot. Radiat.*, 2013, **20**, 234-242.
25. B. Ravel and M. Newville, *J. Synchrot. Radiat.*, 2005, **12**, 537-541.
26. J. J. Rehr and R. C. Albers, *Rev. Mod. Phys.*, 2000, **72**, 621-654.
27. J. J. Rehr, J. J. Kas, M. P. Prange, A. P. Sorini, Y. Takimoto and F. Vila, *C. R. Phys.*, 2009, **10**, 548-559.
28. R. Tauler, *Chemometrics Intell. Lab. Syst.*, 1995, **30**, 133-146.
29. R. Tauler, A. Smilde and B. Kowalski, *J. Chemometr.*, 1995, **9**, 31-58.
30. J. Jaumot, A. de Juan and R. Tauler, *Chemometrics Intell. Lab. Syst.*, 2015, **140**, 1-12.
31. A. March, *Z. Kristall.*, 1932, **81**, 285-297.
32. E. J. Frazer and S. Phang, *J. Power Sources*, 1981, **6**, 307-317.
33. H. S. Ryu, J. S. Kim, J. S. Park, J. W. Park, K. W. Kim, J. H. Ahn, T. H. Nam, G. X. Wang and H. J. Ahn, *Journal of the Electrochemical Society*, 2013, **160**, A338-A343.
34. F. Farges, G. E. Brown and J. J. Rehr, *Geochimica Et Cosmochimica Acta*, 1996, **60**, 3023-3038.

35. D. Zhou, S. Permien, J. Rana, M. Krengel, F. Sun, G. Schumacher, W. Bensch and J. Banhart, *Journal of Power Sources*, 2017, **342**, 56-63.
36. W. Zhang, M. Topsakal, C. Cama, C. J. Pelliccione, H. Zhao, S. Ehrlich, L. J. Wu, Y. M. Zhu, A. I. Frenkel, K. J. Takeuchi, E. S. Takeuchi, A. C. Marschilok, D. Y. Lu and F. Wang, *J. Am. Chem. Soc.*, 2017, **139**, 16591-16603.
37. M. Maeder, *Anal. Chem.*, 1987, **59**, 527-530.
38. H. R. Keller and D. L. Massart, *Chemometrics Intell. Lab. Syst.*, 1992, **12**, 209-224.
39. K. Momma and F. Izumi, *J. Appl. Crystallogr.*, 2011, **44**, 1272-1276.
40. K. Cenzual, L. M. Gelato, M. Penzo and E. Parthe, *Acta Crystallogr. Sect. B-Struct. Commun.*, 1991, **47**, 433-439.
41. M. D. Radin and A. Van der Ven, *Chemistry of Materials*, 2016, **28**, 7898-7904.
42. X. Z. Wang, Z. P. Yao, S. Hwang, Y. Pan, H. Dong, M. S. Fu, N. Li, K. Sun, H. Gan, Y. Yao, A. Aspuru-Guzik, Q. Y. Xu and D. Su, *ACS Nano*, 2019, **13**, 9421-9430.

Operando Structural and Chemical Evolutions of TiS_2 in Na-ion Batteries

Cheng-Hung Lin[1], Mehmet Topsakal[2], Ke Sun[1, 3], Jianming Bai[4], Chonghang Zhao[1], Eric Dooryhee[4], Paul Northrup[5], Hong Gan[3], Deyu Lu[6], Eli Stavitski[4], Yu-chen Karen Chen-Wiegart[1, 4]

1. Department of Materials Science and Chemical Engineering, Stony Brook University, Stony Brook, NY 11794

2. Nuclear Science and Technology Department, Brookhaven National Laboratory, Upton, NY 11973

3. Sustainable Energy Technologies Department, Brookhaven National Laboratory, Upton, NY 11973

4. National Synchrotron Light Source II, Brookhaven National Laboratory, Upton, NY 11973

5. Department of Geosciences, Stony Brook University, Stony Brook, NY, 11794

6. Center for Functional Nanomaterials, Brookhaven National Laboratory, Upton, NY 11973

Combination of multi-modal synchrotron approach and data analytics furthers understanding of electrochemically driven phase-transformation of TiS_2 in Na-ion batteries.